Data in Brief 5 (2015) 626–641

Contents lists available at ScienceDirect

Data in Brief

journal homepage: www.elsevier.com/locate/dib

Data Article

Data analysis and other considerations concerning the study of precipitation in Al–Mg–Si alloys by Atom Probe Tomography

M.W. Zandbergen [a,*], Q. Xu [b], A. Cerezo [a], G.D.W. Smith [a]

[a] Department of Materials, University of Oxford, Parks Road, Oxford OX1 3PH, UK
[b] National Center for HREM, Kavli Institute of Nanoscience, Delft University of Technology, Lorentzweg 1, NL-2628 CJ Delft, The Netherlands

ARTICLE INFO

Article history:
Received 19 August 2015
Received in revised form
8 September 2015
Accepted 29 September 2015
Available online 9 October 2015

ABSTRACT

Atom Probe Tomography (APT) analysis and hardness measurements were used to characterize the early stages of precipitation in an Al–0.51 at%Mg–0.94 at%Si alloy as reported in the accompanying Acta Materialia paper [1]. The changes in microstructure were investigated after single-stage or multi-stage heat treatments including natural ageing at 298 K (NA), pre-ageing at 353 K (PA), and automotive paint-bake ageing conditions at 453 K (PB). This article provides Supporting information and a detailed report on the experimental conditions and the data analysis methods used for this investigation. Careful design of experimental conditions and analysis methods was carried out to obtain consistent and reliable results. Detailed data on clustering for prolonged NA and PA treatments have been reported.

Specifications Table

Subject area	*Materials Science*
More specific subject area	*Nanostructure, metallurgy, precipitation, aluminium alloys*

DOI of original article: http://dx.doi.org/10.1016/j.actamat.2015.08.017
* Corresponding author at: Consultant, Lux Research Inc, 100 Franklin Street, 8th Floor, Boston, MA 02110. Tel.: +1 857 284 5681.
E-mail address: mathijsz@gmail.com (M.W. Zandbergen).

http://dx.doi.org/10.1016/j.dib.2015.09.045
2352-3409/

Type of data	*Table, image (APT, TEM), figure*
How data was acquired	*ATP, LEAP* *ATP, LAR-3DAP* *TEM, FEI Tecnai microscope*
Data format	*Analyzed*
Experimental factors	*Heat treatments at* 298 K, 353 K *and* 453 K
Experimental features	*Heat treatments were performed in an air furnace or oil bath. Samples for APT were made by electropolishing*
Data source location	*Department of Materials, Oxford University, Parks Road, Oxford, UK*
Data accessibility	*Data is in this article*

Value of the data

- The description of how the type of APT and the experimental settings influence detection of clusters and precipitation will be useful when comparing results obtained between different APT apparatus.
- Detailed description of which experimental parameters influence detection of clusters in ternary Al–Mg–Si by APT will help the community to design new experiments to measure precipitation in ternary Al–Mg–Si.
- The characterisation of the size and number density of precipitates and clusters during long ageing times may be used by the community to validate microstructure evolution models.
- The variation in composition of the precipitates and clusters can be used by the community to validate thermodynamic and kinetic databases for the Al–Mg–Si system.

1. Data, experimental design, materials and methods

1.1. Characteristics of the different stages of the precipitation in Al–Mg–Si alloys

See Table 1.

1.2. Experimental design

1.2.1. Heat treatments and techniques

The composition of the investigated ternary Al–Mg–Si alloy is shown in Table 2. Sheets were cold-rolled to 1 mm thickness. All heat treatments were performed in an air furnace unless stated

Table 1
Characteristics of phases observed in Al–Mg–Si alloys as reported in the literature.

Type	Composition[a]	Unit cell	Morphology	Ref.
Clusters	Mg/Si: 1–2	–	Spherical	[2–16]
GP zones/ Initial β″/ Pre- β″	$Mg_xAl_{5-x}Si_6$ or $Mg_{2+x}Al_{7-x-y}Si_{2+y}$	Monoclinic, C2/m, $a=1.48$, $b=0.405$, $c=0.648$ nm; $\beta=105.3°$	Spherical 1–3 nm/needles of $2\times2\times20$ nm	[17–23]
β″	Mg_5Si_6	Monoclinic, C2/m, $a=1.516$, $b=0.405$, $c=0.674$ nm; $\beta=105.3°$	Needles of $\sim4\times4\times50$ nm	[24–26]
β′	$Mg_{1.8}Si$	Hexagonal, $P6_3$, $a=0.715$, $c=0.405$/ 1.215 nm; $\gamma=120°$	Needles > 100 nm long, 10 nm in diameter	[18,20,27]
U1 (Type A)	$MgAl_2Si_2$	Trigonal, P_{-3m1}, $a=0.405$, $c=0.674$ nm; $\gamma=120°$	Needles > 100 nm long, 15 nm in diameter	[20,28,29]
U2 (Type B)	MgAlSi	Orthorhombic, P_{nma}, $a=0.675$, $b=0.405$, $c=0.794$ nm	Needles > 100 nm long, 15 nm in diameter	[20,29]
B′ (Type C)	$Mg_9Al_3Si_7$	Hexagonal, $a=1.03$ nm, $c=0.405$ nm	Lath-shaped	[30]
β	Mg_2Si	FCC, CaF, $a=0.639$ nm	Plates or Cubes of 10–20 μm	[31,32]

[a] The Al content of the early-stage phases is very difficult to determine and is therefore not given here.

Table 2
Composition of the alloy in wt% and at%.

	Al	Si	Mg	Cu	Fe	Mn
(wt%)	Balance	0.98 ± 0.02	0.46 ± 0.01	0.029 ± 0.002	0.17 ± 0.01	0.10 ± 0.02
(at%)	Balance	0.94 ± 0.02	0.51 ± 0.01	0.013 ± 0.001	0.08 ± 0.01	0.05 ± 0.01
Measured by APT						
(at%)	Balance	0.95 ± 0.01	0.46 ± 0.01	0.016 ± 0.001	–	0.03 ± 0.01

Table 3
Heat treatments.

Heat treatment	
1 min NA+PB	1 min natural ageing at 298 K+10 min, 30 min, 4 h, 18 h, 400 h, or 580 h ageing at 453 K
NA	100, 1000 and 10,000 min natural ageing at 298 K
PA (+ NA)	2 h, 10 h or 1 week pre-ageing at 353 K (+ 1 week natural ageing at 298 K)
Spike+PA+NA	10 s at 453 K+2 h or 10 h pre-ageing at 353 K+1 week natural ageing at 298 K
NA+PB	1 min, 10 min, 100 min or 1 week natural ageing at 298 K+30 min ageing at 453 K
2 or 10 h PA+1 week NA+PB	2 h or 10 h pre-ageing at 353 K+1 week natural ageing at 298 K+30 min ageing at 453 K
Spike+2 h PA+NA+PB	10 s at 453 K+2 h or 10 h pre-ageing at 353 K+1 week natural ageing at 298 K+30 min ageing at 453 K

otherwise. The samples were solid solution heat-treated (SSHT) at 835 K for 30 min followed by a water quench to room temperature. Following SSHT, single or multi-stage ageing treatments were performed at 298 K (NA), 353 K (PA) and 453 K (PB). For multi-stage heat treatments including a PB treatment, the PB time was kept constant at 30 min. The precursor stages were systematically varied to mimic the different stages of industrial production. In some cases a transient heat treatment in an oil bath (referred to as a spike) was given for 10 s at 453 K before PA. The spike was given 1 min after the solid solution heat treatment (SSHT), and 2 min before PA. After the spike the material was water-quenched. Keeping the times constant between SSHT and the ageing treatments was important to get reproducible results. PB or PA treatments were commenced 1 or 3 min after the water quench, respectively. If necessary, the material was stored in liquid nitrogen after heat treatments to inhibit the influence of any subsequent NA. The various heat treatments are listed in Table 3.

Hardness measurements were carried out using a calibrated Vickers indenter at a 2 kg load and an indentation time of 10 s. 5 measurements were carried out across each sample to give a mean hardness value. The experimental error was estimated by dividing the standard deviation value by the square root of the number of measurements.

Needle-shaped specimens for APT experiments were made by a standard electropolishing method [33] from heat-treated thin bars by applying 10–15 V on the specimen in a 25% perchloric acid (65%) and 75% acetic acid (100%) solution at 278 K. These tips were then back-polished when necessary in a solution of 2% perchloric acid (65%) in 2-butoxyethanol. For APT analysis, two different types of 3D atom probe were used, a local-electrode atom probe (LEAP™) [34,35] and a large-angle-reflectron 3D atom probe (LAR-3DAP™) [36]. Analyses were carried out at specimen temperatures of 25–30 K and pulse voltages of 15–20% of the standing DC voltage.

1.2.2. APT analysis

Multiple samples were analysed for each heat treatment wherever possible. The size, morphology, and number density of the particles and the matrix compositions were extracted from the APT data by using particle selection software in PoSAP™ and IVAS™. Solute atoms (Mg and Si) were identified to be part of the same particle when they were within a maximum linear separation distance, d, from each other. A second parameter N_{min} was used, defined as the minimum number of solute atoms a particle had to contain for it to be identified as such. When a particle has fewer than N_{min} solute atoms, it was

disregarded. Values of d and N_{min} were chosen so that no artefact solute "particles" were observed in a random solid solution of the same alloy composition. These values were determined by randomly assigning atom identities to the experimentally-observed positions in data sets and testing different N_{min} and d values on these randomized data. For LEAP measurements, a d of 0.65 nm and N_{min} of 10 solute atoms was used. As N_{min} was set at 10, particles smaller than 10 detected solute atoms were not selected. A d of 0.70 nm was allowed for LAR-3DAP measurements due to the lower detection efficiency of the LAR-3DAP (35% versus 50% for the LEAP). It should be noted that, due to these limited detection efficiencies, the particles contained 2–2.86 times as many solute atoms in reality as were detected in this work. The average size as detected by LAR-3DAP was adjusted by multiplying by 0.50/0.35 to correct for the difference in detection efficiency between LEAP and LAR-3DAP.

In some cases, further particle analysis was carried out using a N_{min} of 5. Lowering N_{min} and leaving d constant leads statistically to the selection of artefact "particles" in datasets with a random solute distribution. To take this into account, the relevant datasets were randomized to find the number density of artefact "particles" in the equivalent random solute distribution using a N_{min} of 5. An estimated number density for real particles consisting of more than 5 solute atoms was then calculated from the difference in number density between original and randomized datasets.

IVAS™ software was used to determine the dimensions of each particle measured along three orthogonal axes, x, y, and z. This analysis was only carried out on particles found using the parameters $d=0.65$ and $N_{min}=70$ for LEAP measurements. The precipitate length corresponded to the longest (z) axis, e.g. the elongated direction of a β'' precipitate. For lath-shaped precipitates, the shortest (x) axis indicated the depth of the precipitates, whereas the (y) axis indicated the width of precipitates. The shortest (x) axis was used to indicate the diameter of particles that were needle-shaped. The statistical errors for number density of particles and particle Mg/Si ratios were calculated assuming a Poisson distribution for the particle population [33].

The measured overall solute concentrations by APT are shown in Table 2. The Mg concentration is underestimated by about 10%. The statistical error for the measured solute concentrations, based on the number of atoms in the dataset, was 0.01–0.02 at%. However, the systematic error was higher due to minor sample-to-sample composition variations and differences in experimental conditions and was estimated to be around 0.05 at%. The mean particle size was defined as the average number of solutes atoms in the particles. The error for this value was estimated by dividing the standard deviation of mean particles size by the square root of the number of particles. The statistical error for the average particle dimensions was similarly estimated by dividing standard deviation of average particle length by the square root of the number of particles.

Determination of the number density of particles according to their length was sometimes difficult, because some particles were cut off at the edges of the analysis. To take this into account, particles shorter than 6 nm or containing fewer than 100 solute atoms as measured by LEAP and cut off at the edges were discarded. To characterize the length of particles after 580 h PB (when the length of particles could not be determined by APT), transmission electron microscopy (TEM) was performed on a needle-shaped APT sample using a FEI Tecnai microscope at TU Delft.

1.2.3. APT considerations

It should be noted that LEAP and LAR-3DAP measurements can give differences in results with respect to particle chemistry (by 20–30%) and number density (by 10–60%), especially in the cases of the very smallest particles [37]. These variations are due to differences in overall detection efficiency, field-of-view and mass resolution for the two types of atom probe. However, the trends in the data are the same in both atom probes. In general, the particle chemistries and number densities reported here are those detected by LEAP, to ensure full compatibility between data sets. The applied DC voltage also has a large influence on detection of these particles as the detected number density for the very smallest particles (containing fewer than 40 solute atoms) can decrease by as much as 20–30% with 1 kV of increase in voltage, due to limitations in spatial resolution [37]. Comparison of number densities of small particles was therefore only performed for measurements at similar low voltages (below 6 kV and within a 1 kV range).

Table 4 shows that the presence of large elongated particles ($>$ 15 nm) after prolonged PB led to a lower apparent overall solute concentration relative to the bulk alloy composition (decrease of 0.08–

Table 4
Lower detected overall solute concentration by LEAP after 30 min or 18 h ageing at 453 K.

	Mg	Si
Average overall Mg and Si concentrations of measurements after NA or PA (at%)[a]	0.46 ± 0.01	0.95 ± 0.01
Overall Mg and Si concentrations of measurement after 30 min PB[b] (at%)	0.36 ± 0.01	0.77 ± 0.01
Loss of Mg and Si atoms in 30 min PB measurement (at%)	**0.10**	**0.18**
Overall Mg and Si concentrations of measurement after 18 h PB[b] (at%)	0.34 ± 0.01	0.79 ± 0.01
Loss of Mg and Si atoms in 18 h PB measurement (at%)	**0.12**	**0.16**

[a] The average overall composition of 10 LEAP measurements after NA or PA. These datasets only contain clusters (particles containing fewer than 70 solute atoms).
[b] Mainly elongated precipitates longer than 15 nm are present.

Table 5
Estimation of precipitate Mg/Si ratio compensating for the loss of Si and Mg atoms during APT analysis.

	Mg	Si
Average overall Mg and Si concentrations of measurements after NA or PA (at%)[a]	0.46 ± 0.01	0.95 ± 0.01
Matrix Mg and Si concentrations of measurement after 30 min PB[b] (at%)	0.16 ± 0.01	0.62 ± 0.01
Estimated amount of solutes in elongated precipitates in 30 min PB measurement (at%)	**0.30**	**0.33**
Estimated average precipitate Mg/Si ratio	**0.91**	
Average precipitate Mg/Si ratio as measured by LEAP	**1.35**	
Matrix Mg and Si concentrations of measurement after 18 h PB[b] (at%)	0.09 ± 0.01	0.60 ± 0.01
Estimated amount of solutes in elongated precipitates in 18 h PB measurement (at%)	**0.37**	**0.35**
Estimated average precipitate Mg/Si ratio	**1.06**	
Average precipitate Mg/Si ratio as measured by LEAP	**1.35**	

[a] The average overall composition of 10 LEAP measurements after NA or PA. These datasets only contain clusters (particles containing fewer than 70 solute atoms).
[b] Mainly elongated precipitates longer than 12 nm are present.

0.12 at% for Mg and 0.15–0.20 at% for Si). This is thought to occur due to failure in the detection of multiple ions evaporating per pulse from these larger precipitates [37–40]. Relatively more Si atoms were undetected than Mg atoms. When the losses of Si and Mg were taken into account, the average Mg/Si ratios of large elongated particles (> 15 nm) were estimated to be in the range of 0.90 and 1.05 as shown in Table 5. This is close to the Mg/Si ratio of Mg_5Si_6, but lower than the values of 1.2–1.4 found by APT without taking the losses of Mg and Si into account. In the other sections, only the unadjusted particle Mg/Si ratios as measured by APT are given. The average particle Mg/Si ratios of datasets containing large elongated particles (> 15 nm) are therefore overestimated by 20–40% in this section. It should also be noted that local aberration effects due to ion trajectory differences between different phases [33] increase the apparently-measured width of the interface between matrix and precipitates by 2–3 nm. Only the apparent widths are given in the subsequent sections.

To estimate the relative Al content in particles, composition profiles of elongated particles were obtained by plotting a proximity histogram (proxigram) from isoconcentration surfaces defined so as to mark the matrix/particle interface [33]. An isosurface is a 3-D contour surface passing through all points of a particular solute concentration range. A 6–8 at% (Mg + Si) concentration value was used for

large particles (average length >15 nm) and a 4–6 at% value for smaller particles (average length <15 nm). The delocalisation (smoothing) parameter was set at 3–5 nm.

1.3. Prolonged ageing

1.3.1. Prolonged PB

The data shown here are complimentary to the results discussed in the accompanying Acta Materialia paper [1]. Distributions of the diameter and the detected precipitate Mg/Si ratio against the precipitate length are plotted in Fig. 1. From the APT analysis observations, there is no clear distinction between the successive phases, the change in precipitate length being continuous. The diameter increases from 3–4 nm for short-elongated precipitates to 5–6.5 nm for precipitates longer than 15 nm. The diameter of the precipitates increases only slightly (by <1 nm) as they grow longer than 15 nm, demonstrating that the large needle-shaped precipitates hardly coarsen laterally with increasing ageing time.

Ageing for 580 h at 453 K gives precipitates of 100–200 nm in length as shown in the TEM image in Fig. 2. APT measurements show that these precipitates are lath-shaped. The precipitates have probably transformed into B′, which has a proposed composition of $Mg_9Al_3Si_7$ [30,41]. The proposed B′ Mg/Si ratio of 1.29 is close to that found here after adjusting for the preferential loss of solutes (1.55–1.75 as measured by APT to 1.0–1.4 after adjustment for loss of Mg and Si atoms).

After prolonged PB, the solute matrix concentrations decrease to below 0.05 at%. Fig. 3 shows that extrapolations of solid solubility limits at temperatures above 498 K known from the literature [42] coincide with the measured matrix concentrations after 580 h PB. This demonstrates that the solid solubility limits of Mg and Si are below 0.05 at% at 453 K in ternary Al–Mg–Si, meaning that 0.48 at% Mg and 0.89 at% Si have come out of solution. The B′ precipitates are Mg-rich, showing that 0.4–0.6 at% Si is not accounted for. Consequently, it is possible that large Si-rich precipitates have formed,

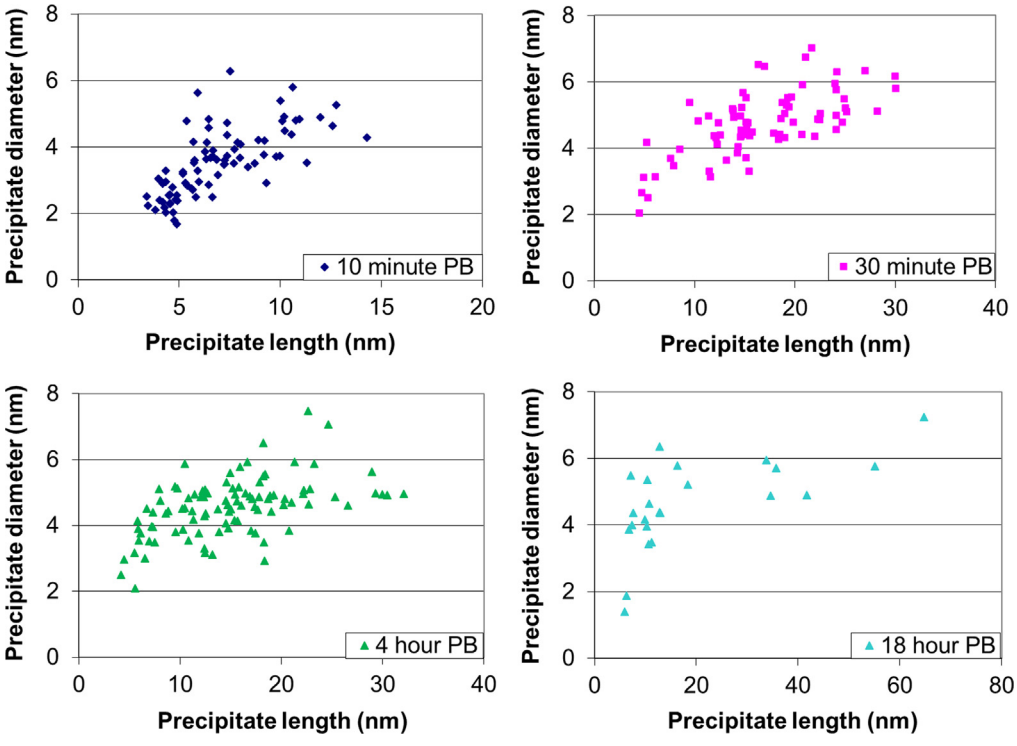

Fig. 1. Measured diameters of precipitates plotted against precipitate length after various PB treatments at 453 K.

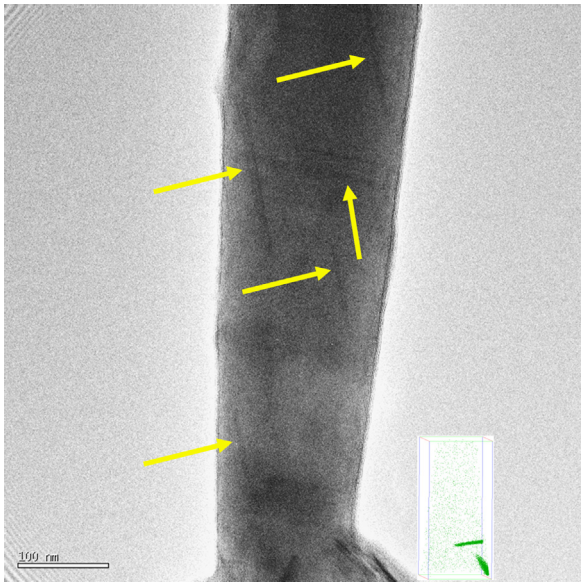

Fig. 2. TEM image of APT specimen heat treated for 1 min at room temperature and 580 h at 453 K. The yellow arrows indicate elongated B′ precipitates. The inset is a LAR-3DAP measurement of the same material at the same magnification, but not the same area of analysis.

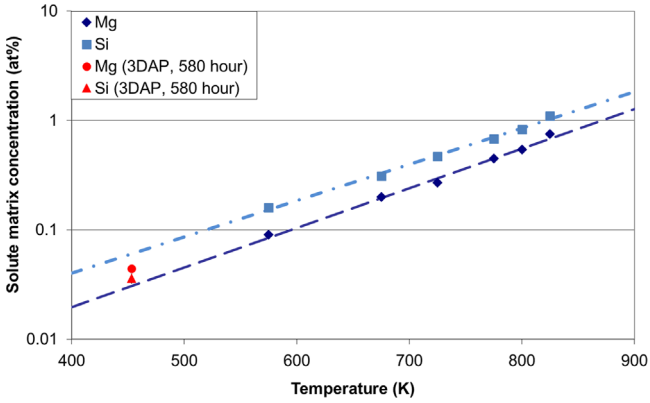

Fig. 3. Solid solubility limits (in at%) of Mg and Si in aluminium in Al–Mg–Si system. Values on the dark blue and pink lines are from [42].

as has been reported to occur in excess-Si Al–Mg–Si alloys after prolonged ageing at 453 K (> 100 h) [43,44]. The Si diffusion distances at equilibrium vacancy concentrations are estimated to be above 700 nm for 400 h ageing at 453 K [45]. Although large Si precipitates have not been observed in the APT measurements, it is possible that they were formed during prolonged PB as the longest experimental run was only 60 nm wide and 350 nm in length.

1.3.2. Prolonged NA

The data shown here are complimentary to the results discussed in the accompanying Acta Materialia paper [1]. Detailed APT data after prolonged NA by LAR-3DAP are shown in Table 6 and Fig. 4. After 11 or 48 weeks of NA, the cluster number density is stable. The clusters grow in size from

Table 6
LAR-3DAP measurements after 1, 11 or 48 week NA.

NA time	Average cluster size (number of solute atoms)	Cluster Mg/Si ratio[a]	Cluster number density ($\times 10^{22}/m^3$) $N_{min}=10$	Cluster number density ($\times 10^{22}/m^3$) $N_{min}=5$
1 week NA	13.9 ± 0.5	0.86 ± 0.03	120 ± 13	400 ± 50
11 week NA	17.8 ± 0.9	0.87 ± 0.02	341 ± 21	490 ± 50
48 week NA	16.4 ± 0.8	0.95 ± 0.03	223 ± 19	400 ± 50

[a] The variations in cluster chemistry are assumed to be mainly caused by the differences in measured overall composition.

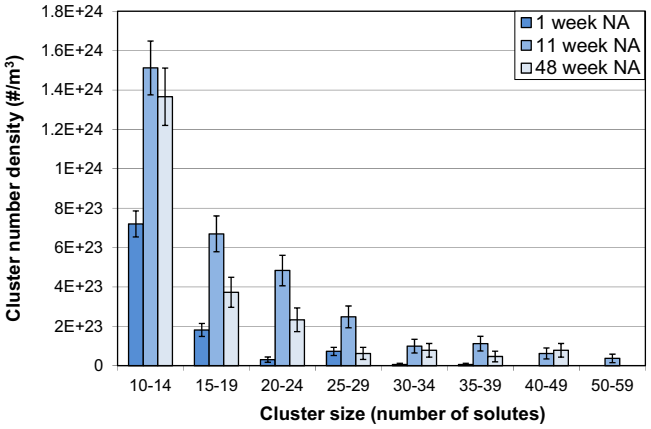

Fig. 4. Cluster number densities for different cluster size ranges after 1, 11 or 48 weeks NA as measured by LAR-3DAP. The cluster sizes were obtained using a N_{min} of 10 for cluster analysis.

1 week to 11 weeks NA. The average cluster Mg/Si ratio and cluster Mg/Si ratio distributions do not change.

1.3.3. Prolonged PA

APT data after prolonged PA by LAR-3DAP are shown in Table 7 and Figs. 5 and 6. Clusters continue to increase in size from 2 h to 1 week PA. After 2 h PA, the cluster number density as measured by LAR-3DAP hardly increases with PA time ($<25\%$), but the average cluster size does by 60% from 2 h to 1 week PA.

1.3.4. Spike and prolonged pre-ageing

APT measurements show that application of a spike (10 s at 453 K) before PA leads to larger clusters with similar Mg/Si ratios to those formed without a spike. Similar to the results by LEAP as discussed in the accompanying Acta Materialia paper [1], LAR-3DAP measurements show that application of a spike before PA leads to larger clusters with similar Mg/Si ratios to those formed without a spike, as illustrated in Table 7 and Figs. 7 and 8. After 1 week PA, clusters are identical in size, morphology and chemistry to the spheroidal precipitates present after PB, as shown in Figs. 9 and 10. Therefore, applying a spike has two effects: it increases the number density of larger clusters which are close in size and chemistry to spheroidal precipitates and it decreases the number density of smaller ones.

Table 7
LAR-3DAP measurements after 2 or 10 h or 1 week PA with and without a spike.

Heat treatment	Average particle size (number of solute atoms)	Particle Mg/Si ratio[a]	Cluster[b] number density ($\times 10^{22}/m^3$)	Precipitate[b] number density ($\times 10^{22}/m^3$)
Without spike				
2 h *PA*	18.2 ± 2.4	1.02 ± 0.05	186 ± 30	–
10 h *PA*	22.0 ± 0.7	0.93 ± 0.02	184 ± 11	9 ± 2
1 *week PA*	28.6 ± 2.1	1.06 ± 0.03	197 ± 18	24 ± 6
With spike				
Spike 2 h *PA* 1 *week NA*	26.7 ± 1.6	0.98 ± 0.03	184 ± 18	29 ± 8
Spike 10 h *PA* 1 *week NA*	34.2 ± 2.0	1.11 ± 0.02	108 ± 10	17 ± 4
Spike 1 *week PA*	45.6 ± 1.8	1.19 ± 0.01	116 ± 10	72 ± 7

[a] The variations in cluster chemistry are assumed to be mainly caused by the differences in measured overall composition.
[b] Precipitates are particles containing more than 50 solute atoms as measured by LAR-3DAP, clusters contain fewer than 50 solute atoms (N_{min} was 10 for particle analysis).

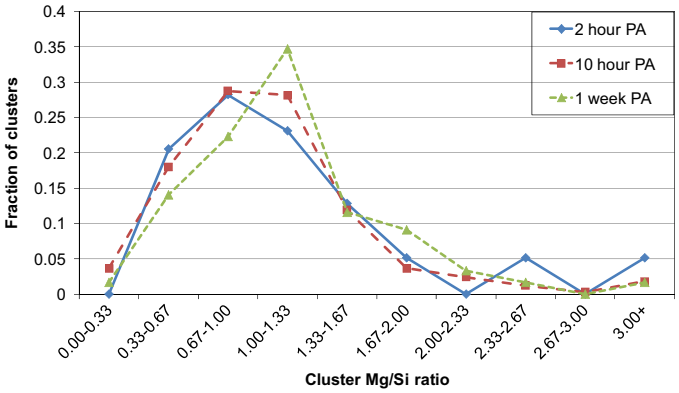

Fig. 5. Fraction of clusters plotted against cluster Mg/Si ratio ranges after 2 or 10 h or 1 week PA as measured by LAR-3DAP.

1.3.5. Clusters after PB

The effects of ageing at 453 K after NA and PA on clusters and precipitation is discussed in the accompanying Acta Materialia paper [1]. Table 8 summarises the change in number densities of clusters and precipitates after different heat treatments. Not every cluster formed during PA grows into an elongated precipitate upon subsequent PB. For 10 h PA, the decrease in number density of small clusters is $\sim 90 \times 10^{22}/m^3$ during PB, whereas the increase in precipitates containing more than 70 solute atoms is only $20–30 \times 10^{22}/m^3$. Clusters present after a 10 or 30 min PB have a Mg/Si ratio of 0.9–1.2, which is comparable to that of clusters present after PA before the PB and to that of precipitates formed during the PB.

1.4. Additional data after multiple heat treatments

1.4.1. Effect of pre-ageing on the paint-bake

The data shown here is complimentary to the results discussed in the accompanying Acta Materialia paper [1]. When PA is given prior to NA, the change in hardness during 1 week NA is significantly reduced. The hardness is 55–60 H_v after 2 h PA and increases to 60–67 H_v after 1 week NA. 10 h PA leads to a hardness of 67 ± 1 H_v, which hardly increases during 1 week of NA.

PA partially mitigates the deleterious effects of subsequent 1 week NA as illustrated in the hardness plots in Fig. 11. The hardness increases by approximately 30 H_v after 30 min PB when PA is

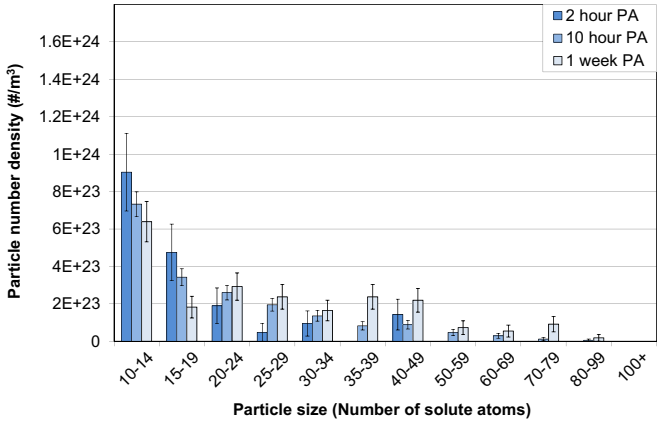

Fig. 6. Particle number densities for different particle size ranges after 2 or 10 h or 1 week PA as measured by LAR-3DAP. A N_{min} of 10 was used for particle analysis.

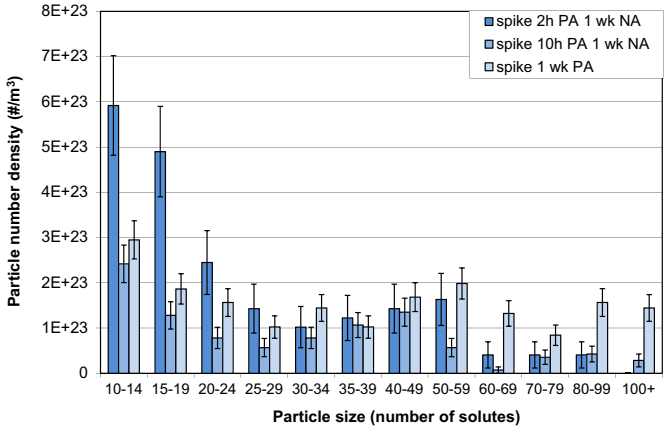

Fig. 7. Particle number densities for different particle size ranges after a spike and 2 or 10 h or 1 week PA as measured by LAR-3DAP. A N_{min} of 10 was used for particle analysis.

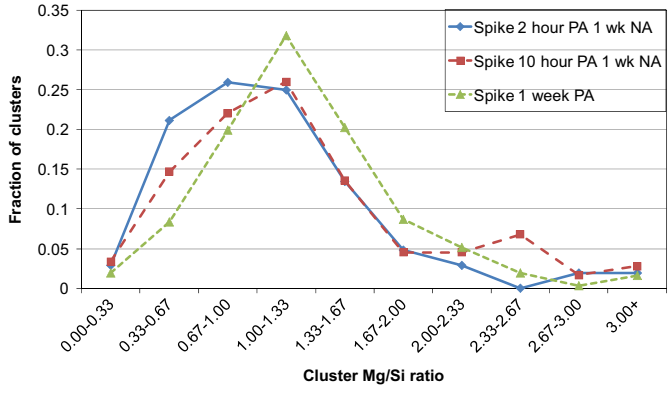

Fig. 8. Fraction of clusters plotted against cluster Mg/Si ratio ranges after a spike followed by 2 or 10 h or 1 week PA as measured by LAR-3DAP.

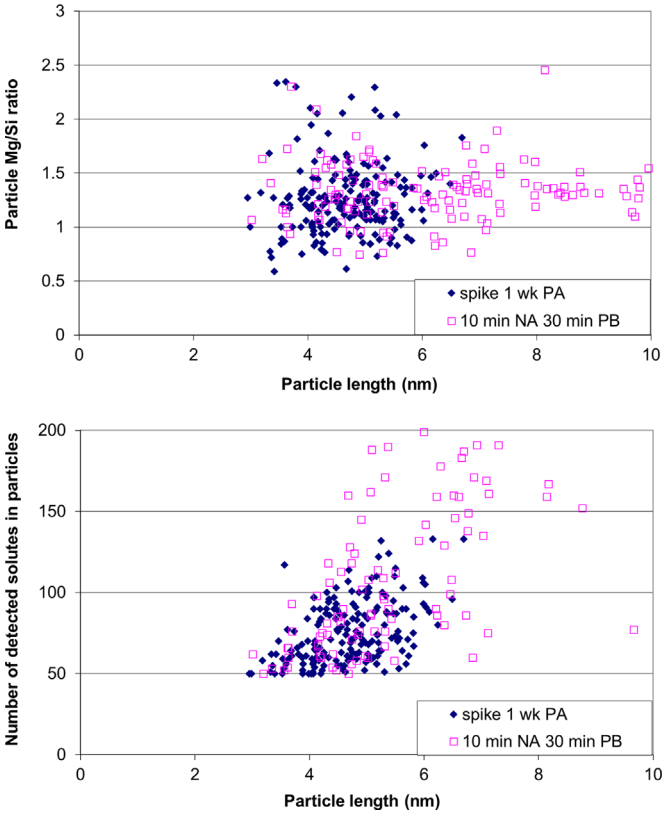

Fig. 9. Particle Mg/Si ratio or number of detected solute atoms in particles plotted against particle length after a spike and 1 week PA (blue) or 10 min NA and 30 min PB (pink) as measured by LAR-3DAP. Only particles consisting of 50 solute atoms or more are taken into account. The particle sizes and compositions were obtained using a N_{min} of 10 for particle analysis.

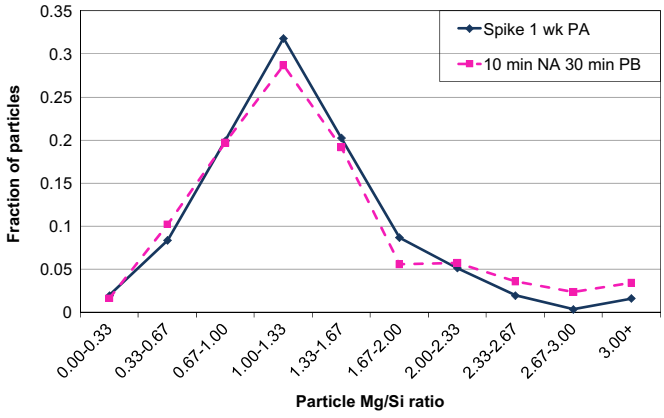

Fig. 10. Fraction of particles containing fewer than 150 solute atoms plotted against particle Mg/Si ratio ranges after a spike followed by 1 week PA or after 10 min NA and a 30 min PB as measured by LAR-3DAP.

Table 8
Number densities of particles containing 10–20, 20–40, 40–70 and 70+ solute atoms as measured by LEAP after different heat treatments using a N_{min} of 10.

Heat treatment	Number density clusters of 10–20 solute atoms ($\times 10^{22}/m^3$)	Number density clusters of 20–40 solute atoms ($\times 10^{22}/m^3$)	Number density clusters of 40–70 solute atoms ($\times 10^{22}/m^3$)	Number density precipitates 70+ solute atoms ($\times 10^{22}/m^3$)
1 min NA				
10 min PB[a]	34 ± 3	22 ± 3	10 ± 2	26 ± 2
30 min PB	4.7 ± 0.7	1.2 ± 0.4	0.7 ± 0.3	13 ± 1
1 week NA				
Before PB	101 ± 6	15 ± 2	–	–
30 min PB	85 ± 5	30 ± 3	2 ± 1	1 ± 1
10 h PA 1 week NA				
Before PB	85 ± 12	73 ± 11	13 ± 5	1 ± 1
10 min PB	45 ± 4	26 ± 3	17 ± 3	24 ± 3
30 min PB	45 ± 3	21 ± 2	9 ± 1	30 ± 2
Spike 2 h PA 1 week NA				
Before PB	59 ± 5	26 ± 3	12 ± 2	3 ± 1
30 min PB	24 ± 2	12 ± 2	9 ± 1	27 ± 3

[a] This was measured at 1–2 kV lower voltage than the other measurement.

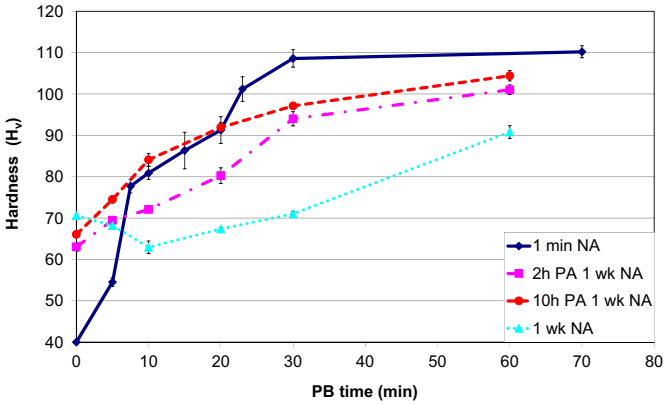

Fig. 11. Change in hardness with PB time after 1 min NA or 1 week NA when no PA is given or when 2 or 10 h of PA is given prior to NA.

given, which is lower than the 64 ± 3 H_v increase when the PB is given 1 min after the SSHT, but better than the PB response after NA without PA. 1 week NA after 2 h PA has little effect on the PB response, i.e. hardly any difference is seen in the hardness curves after 2 h PA with and without 1 week NA. Increasing the PA time to 10 h improves the hardening response by 5–10 H_v during the first 20 min of PB.

When PA is given, the PB response is slower than when the PB is given directly after the SSHT. After 10 min PB, the microstructure is comparable due to the fact that clusters, precursors to the elongated precipitates, are already present when PA is given. However, precipitates grow considerably faster between 10 and 30 min PB when the NA time is restricted to 1 min as shown in Fig. 12.

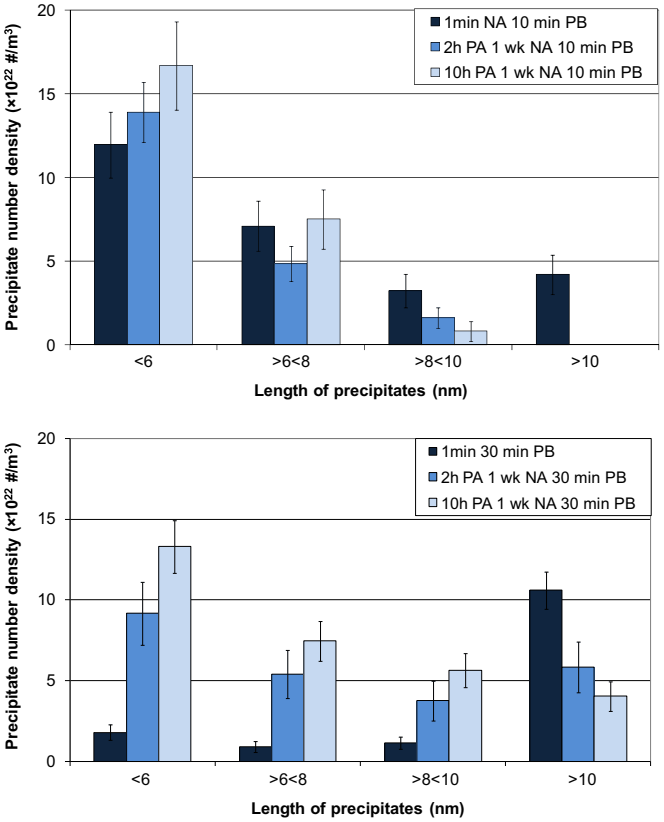

Fig. 12. Number density of precipitates for different precipitate lengths after 1 min NA and a 10 or 30 min PB; 2 h PA 1 week NA and a 10 or 30 min PB; or 10 h PA 1 week NA and a 10 or 30 min PB.

1.5. Calculation of the nucleation barrier after NA

After 100 min NA, the percentage of total Mg atoms of the alloy in clusters is limited to 5–6%. It should be noted that the percentage of Mg in clusters might be underestimated as some clusters are too small to be detected by APT. If we make a conservative estimate that we only measure a third of the smallest clusters then 15–18% of Mg should be in clusters, corresponding to a decrease in the Mg concentration of ~0.08 at%. This decrease in matrix Mg concentration increases the nucleation barrier (ΔG^*). ΔG^* for spherical particles, according to the classical nucleation and growth theory [46], is estimated by: $\Delta G^* = 16\pi\gamma^3/3\Delta g^2$, where Δg is the driving force per unit volume for precipitation, γ the specific interfacial energy between the matrix and cluster or precipitate (between 0.1 and 0.45 J/m^2 for β″ [47]). Δg can be estimated (assuming the strain energy per unit volume is negligible) by: $\Delta g = \Delta g_{chem} = -(k_B T/V_\beta)\ln(C/C_{eq})$, where k_B is the Boltzmann constant (J/K), T the temperature (K), V_β the atomic volume of phase β (m^3) and C_{eq} the equilibrium matrix solute concentration in the solvent. A V_β for the β″ phase is used for all calculations. Table 9 shows the equilibrium matrix solute concentrations for different phases determined by APT in this work. These concentrations have been used to calculate Δg and ΔG^* for clusters with a chemistry close to that of elongated precipitates (PB clusters) as shown in Table 10. Two values for γ, 0.15 or 0.3 J/m^2, have been investigated. The solute concentration decrease in the matrix after 100 min NA leads to an increase of ~20% for ΔG^* for clusters acting as precursors to the elongated phases. The relative change in nucleation rate is calculated by dividing $\exp(-\Delta G^*/k_B T)$ after 100 min NA by that before NA. For both γ values, ΔG^* increases after 100 min NA leading to a decrease in the nucleation rate. It should be noted that the

Table 9
Matrix solute concentrations below which certain phases are not observed at 453 K.

Phase	Matrix Mg concentrations (at%)	Matrix Si concentration (at%)
NA clusters[a]	0.49 ± 0.02	0.92 ± 0.03
PA/PB clusters	0.080 ± 0.002	0.58 ± 0.02
β″	0.043 ± 0.003	0.046 ± 0.006

[a] Clusters dissolve or change chemistry and size upon ageing at 453 K.

Table 10
Estimation of nucleation barriers and the decrease in nucleation rate after 100 min NA.

	γ (J/m^2)		$\Delta g_{chem.}$ (J/m^3)	ΔG^* (J)	Exp(ΔG^*/kT)	Exp(ΔG^*/kT)$_{100\ min NA}$/Exp(ΔG^*/kT)$_{noNA}$
Clusters formed during PB	0.3	Before NA	-7.1×10^8	9.0×10^{-19}	3.4×10^{-63}	1.4×10^{-13}
		100 min NA	-6.5×10^8	1.1×10^{-18}	4.9×10^{-76}	
	0.15	Before NA	-7.1×10^8	1.1×10^{-19}	1.6×10^{-8}	2.5×10^{-2}
		100 min NA	-6.5×10^8	1.4×10^{-19}	3.9×10^{-10}	

values for ΔG^* are reasonable at 0.70 or 0.85 eV when γ is 0.15 J/m^2. This value is comparable to 0.75–0.90 eV (72–87 kJ/mol) as reported by Banhart et al. [48] based positron annihilation lifetime spectroscopy (PALS) measurements. The calculations show that the relatively small changes in matrix solute concentrations after 100 min NA lead to a significant reduction of nucleation of clusters, which develop into larger precipitates.

Acknowledgements

This research was carried out under project number MC4.04191 for the Materials Innovation Institute in the Netherlands (www.m2i.nl), using the APT facilities at Oxford University. LEAP, LAR-3DAP, PoSAP and IVAS are trademarks of Cameca Instruments Inc.

Appendix A. Supplementary material

Supplementary data associated with this article can be found in the online version at http://dx.doi.org/10.1016/j.dib.2015.09.045.

References

[1] M.W. Zandbergen, Q. Xu, A. Cerezo, G.D.W. Smith, Study of precipitation in Al–Mg–Si alloys by atom probe tomography I: microstructural changes as a function of ageing temperature, Acta Mater. 101 (2015) 136–148.
[2] G.A. Edwards, K. Stiller, G.L. Dunlop, M.J. Couper, The precipitation sequence in Al–Mg–Si alloy, Acta Mater. 46 (1998) 3893–3904.
[3] M. Murayama, K. Hono, M. Saga, M. Kikuchi, Atom probe studies on the early stages of precipitation in Al–Mg–Si alloys, Mater. Sci. Eng. A 250 (1998) 127–132.
[4] M. Murayama, K. Hono, Pre-precipitate clusters and precipitation processes in Al–Mg–Si alloys, Acta Mater. 47 (1999) 1537–1548.
[5] M. Murayama, K. Hono, W.F. Miao, D.E. Laughlin, The effect of Cu additions on the precipitation kinetics in an Al–Mg–Si alloy with excess Si, Metall. Mater. Trans. A 32 (2001) 239–246.
[6] S.P. Ringer, K. Hono, Microstructural evolution and age hardening in aluminium alloys: atom probe field-ion microscopy and transmission electron microscopy studies, Mater. Charact. 44 (2000) 101–131.

[7] A. Serizawa, S. Hirosawa, T. Sato, Three-dimensional atom probe characterization of nanoclusters responsible for multistep aging behavior of an Al–Mg–Si alloy, Metall. Mater. Trans. A 39 (2008) 243–251.
[8] J. Buha, R.N. Lumley, A.G. Crosky, K. Hono, Secondary precipitation in an Al–Mg–Si–Cu alloy, Acta Mater. 55 (2007) 3015–3024.
[9] J. Buha, R.N. Lumley, A.G. Crosky, Microstructural development and mechanical properties of interrupted aged Al–Mg–Si–Cu alloy, Metall. Mater. Trans. A 37 (2006) 3119–3130.
[10] F. De Geuser, W. Lefebvre, D. Blavette, 3D atom probe study of solute atoms clustering during natural ageing and pre-ageing of an Al–Mg–Si alloy, Philos. Mag. Lett. 86 (2006) 227–234.
[11] A. Serizawa, T. Sato, W.J. Poole, The characterization of dislocation–nanocluster interactions in Al–Mg–Si(–Cu/Ag) alloys, Philos. Mag. Lett. 90 (2009) 279–287.
[12] A.I. Morley, M.W. Zandbergen, A. Cerezo, G.D.W. Smith, The effect of pre-ageing and addition of copper on the precipitation behaviour in Al–Mg–Si alloys, Mater. Sci. Forum 519–521 (2006) 543–548.
[13] S. Hirosawa, T. Sato, Nano-scale clusters formed in the early stage of phase decomposition of Al–Mg–Si alloys, Mater. Sci. Forum 475–479 (2005) 357–360.
[14] M. Torsæter, H.S. Hasting, W. Lefebvre, C.D. Marioara, J.C. Walmsley, S.J. Andersen, R. Holmestad, The influence of composition and natural aging on clustering during pre-aging in Al–Mg–Si alloys, J. Appl. Phys. 108 (2010) 073527–073529.
[15] G. Sha, H. Möller, W.E. Stumpf, J.H. Xia., G. Govender, S.P. Ringer, Solute nanostructures and their strengthening effects in Al–7Si–0.6 Mg alloy F357, Acta Mater. 60 (2012) 692–701.
[16] S. Wenner, K. Nishimura, K. Matsuda, T. Matsuzaki, D. Tomono, F. Pratt, C.D. Marioara, R. Holmestad, Clustering and vacancy behavior in high- and low-solute Al–Mg–-Si alloys, Metall. Mater. Trans. A 45 (2014) 5777–5785.
[17] J.H. Chen, E. Costan, M.A. van Huis, Q. Xu, H.W. Zandbergen, Atomic pillar-based nanoprecipitates strengthen AlMgSi alloys, Science 312 (2006) 416–419.
[18] C. Ravi, C. Wolverton, First-principles study of crystal structure and stability of Al–Mg–Si–(Cu) precipitates, Acta Mater. 52 (2004) 4213–4227.
[19] M.A. van Huis, J.H. Chen, M.H.F. Sluiter, H.W. Zandbergen, Phase stability and structural features of matrix-embedded hardening precipitates in Al–Mg–Si alloys in the early stages of evolution, Acta Mater. 55 (2007) 2183–2199.
[20] M.A. van Huis, J.H. Chen, H.W. Zandbergen, M.H.F. Sluiter, Phase stability and structural relations of nanometer-sized, matrix-embedded precipitate phases in Al–Mg–Si alloys in the late stages of evolution, Acta Mater. 54 (2006) 2945–2955.
[21] K. Matsuda, H. Gamada, K. Fujii, Y. Uetani, T. Sato, A. Kamio, S. Ikeno, High resolution electron microscopy on the structure of Guinier–Preston zones in an Al-1.6 mass Pct Mg_2Si alloy, Metall. Mater. Trans. A 29 (1998) 1161–1167.
[22] G. Thomas, The ageing characteristics of aluminum alloys-electron transmission studies of Al–Mg–Si alloys, J. Inst. Metals 90 (1961) 57–63.
[23] C.D. Marioara, S.J. Andersen, J. Jansen, H.W. Zandbergen, Atomic model for GP-zones in a 6082 Al–Mg–Si system, Acta Mater. 49 (2001) 321–328.
[24] S.J. Andersen, H.W. Zandbergen, J. Jansen, C. Traeholt, U. Tundal, O. Reiso, The crystal structure of the β'' phase in Al–Mg–Si alloys, Acta Mater. 46 (1998) 3283–3298.
[25] P.M. Derlet, S.J. Andersen, C.D. Marioara, A. Froseth, A first-principles study of the β''-phase in Al–Mg–Si alloys, J. Phys. Condens. Matter 14 (2002) 4011–4024.
[26] H.W. Zandbergen, S.J. Andersen, J. Jansen, Structure determination of Mg_5Si_6 particles in Al by dynamic electron diffraction studies, Science 277 (1997) 1221–1225.
[27] R. Vissers, M.A. van Huis, J. Jansen, H.W. Zandbergen, C.D. Marioara, S.J. Andersen, The crystal structure of the β' phase in Al–Mg–Si alloys, Acta Mater. 55 (2007) 3815–3823.
[28] A.G. Froseth, R. Hoier, P.M. Derlet, S.J. Andersen, C.D. Marioara, Bonding in MgSi and Al–Mg–Si compounds relevant to Al–Mg–Si alloys, Phys. Rev. B 67 (2003) 224106–224109.
[29] S.J. Andersen, C.D. Marioara, R. Vissers, A. Froseth, H.W. Zandbergen, The structural relation between precipitates in Al–Mg–Si alloys, the Al-matrix and diamond silicon, with emphasis on the trigonal phase U1-$MgAl_2Si_2$, Mater. Sci. Eng. A 444 (2007) 157–169.
[30] S. Dumolt, D. Laughlin, J. Williams, Formation of a modified 13″ phase in aluminum alloy 6061, Scr. Metall. 18 (1984) 1347–1350.
[31] A.H. Geisler, J.K. Hill, Analyses and interpretations of X-ray diffraction effects in patterns of aged alloys, Acta Crystallogr. 1 (1948) 238–252.
[32] M.H. Jacobs, The structure of the metastable precipitates formed during ageing of an Al–Mg–Si alloy, Philos. Mag. 26 (1972) 1–13.
[33] M.K. Miller, Atom Probe Tomography: Analysis at the Atomic Level, Kluwer Academic/Plenum Publisher, New York, 2000.
[34] T.F. Kelly, P.P. Camus, D.J. Larson, L.M. Holzman, S.S. Bajikar, On the many advantages of local-electrode atom probes, Ultramicroscopy 62 (1996) 29–42.
[35] T.F. Kelly, D.J. Larson, Local electrode atom probes, Mater. Charact. 44 (2000) 59–85.
[36] P. Panayi, U.K. Patent Application No. GB0509638.3, Nov 15, 2006.
[37] M.W. Zandbergen, Study of Early-Stage Precipitation in Al–Mg–Si(–Cu) Alloys by 3D Atom Probe (DPhil thesis), University of Oxford, 2009.
[38] G. Da Costa, F. Vurpillot, A. Bostel, M. Bouet, B. Deconihout, Design of a delay-line-position-sensitive detector with improved performance, Rev. Sci. Instrum. 76 (2005) 013304–0133048.
[39] H.K. Hasting, W. Lefebvre, C.D. Marioara, J.C. Walmsley, S.J. Andersen, R. Holmestad, F. Danoix, Comparative study of the β''-phase in a 6xxx Al alloy by 3DAP and HRTEM, Surf. Interface Anal. 39 (2007) 189–194.
[40] W. Lefebvre, F. Danoix, G. Da Costa, F. De Geuser, H. Hallem, A. Deschamps, M. Dumont, 3DAP measurements of Al content in different types of precipitates in aluminium alloys, Surf. Interface Anal. 39 (2007) 206.
[41] C. Ravi, C. Wolverton, First-principles study of crystal structure and stability of Al–Mg–Si–(Cu) precipitates, Acta Mater. 52 (2004) 4213–4227.
[42] N. Belov, D. Eskin, A. Aksenov, Multicomponent Phase Diagrams: Applications for Commercial Aluminium Alloys, First ed., Elsevier, Amsterdam, 2005.

[43] C.D. Marioara, S.J. Andersen, H.W. Zandbergen, R. Holmestad, The influence of alloy composition on precipitates of the Al–Mg–Si system, Metall. Mater. Trans. A 36 (2005) 691–702.
[44] L. Zhen, W.D. Fei, S.B. Kang, H.W. Kim, Precipitation behaviour of Al–Mg–Si alloys with high silicon content, J. Mater. Sci. 32 (1997) 1895–1902.
[45] Y. Du, Y.A. Chang, B.Y. Huang, W.P. Gong, Z.P. Jin, H.H. Xu, Z.H. Yuan, Y. Liu, Y.H. He, F.Y. Xie, Diffusion coefficients of some solutes in fcc and liquid Al: critical evaluation and correlation, Mater. Sci. Eng. A 363 (2003) 140–151.
[46] K.C. Russell, Nucleation in solids: the induction and steady state effects, Adv. Colloid Interface Sci. 13 (1980) 205–318.
[47] Y. Wang, Z.K. Liu, L.Q. Chen, C. Wolverton, First-principles calculations of β″-Mg5Si6/α-Al interfaces, Acta Mater. 55 (2007) 5934–5947.
[48] J. Banhart, M.D.H. Lay, C.S.T. Chang, A.J. Hill, Kinetics of natural aging in Al–Mg–Si alloys studied by positron annihilation lifetime spectroscopy, Phys. Rev. B 83 (2011) 014101–014105.